12th International Symposium on Turbulence and Shear Flow Phenomena (TSFP12)
Osaka, Japan (Online), July 19-22, 2022

STATISTICALLY CONSISTENT RESOLVENT-BASED RECONSTRUCTION OF TURBULENT CHANNEL FLOWS FROM LIMITED MEASUREMENTS

Vamsi Krishna Chinta
Aerospace and Mechanical Engineering,
University of Southern California,
Los Angeles, CA 90089.
vchinta@usc.edu

Mitul Luhar
Aerospace and Mechanical Engineering,
University of Southern California,
Los Angeles, CA 90089.
luhar@usc.edu

ABSTRACT

This study develops a resolvent-based framework that can be used to reconstruct the velocity field for turbulent channel flow from limited measurements. For reconstruction, resolvent modes computed at different frequency and wavenumbers are pooled into a large database. The Forward Regression with Orthogonal Least Squares (FROLS) algorithm is used to sequentially identify modes that best represent the input data. A composite loss function is defined with the error for the second-order statistics imposed as a soft constraint to the reconstruction error for velocity field. The amplitude and phase of the identified modes are then optimized to minimize this composite loss function. After calibration, the velocity field can be reconstructed at arbitrary spatiotemporal resolution using the weighted resolvent modes. The resulting model enables estimation of out-of-plane components of velocity and pressure as well as reconstruction in other spanwise locations. For proof-of-concept tests of this method, direct numerical simulation (DNS) data for turbulent channel flow from the Johns Hopkins Turbulence Database (JHTDB) are used. Results indicate that using measurements from multiple planes results in reduced error for the untrained variables (i.e., non-measured velocity components, pressure, out-of-plane data). Using an eddy viscosity model to compute resolvent modes results in smoother statistical profiles, but the velocity field reconstructions do not reproduce small-scale features.

INTRODUCTION

Turbulent flows are characterized by broadbanded fluctuations in the velocity field in both space and time, which makes acquisition of spatiotemporally resolved measurements challenging. For instance, particle image velocimetry (PIV), a standard technique for acquiring spatial velocity fields, is often restricted to a limited field-of-view and not typically time-resolved. Point sensors such as hot-wire anemometers (HWA) can yield time-resolved velocity measurements, but do not provide any spatial information. Previous studies have tried to bridge this gap by reconstructing the flow field between two consecutive PIV snapshots using physics-based models (Krishna *et al.*, 2020) or by using Bayesian inference to fuse non-time-resolved PIV snapshots with time-resolved HWA measurements (Wang *et al.*, 2021). Recent studies have also reconstructed turbulent flow fields from limited measurements using machine learning techniques (e.g., Fukami *et al.*, 2021; Kim *et al.*, 2021).

In this work, we develop a resolvent-based framework for statistically consistent reconstruction of turbulent flows from limited measurements. Specifically, we attempt spatiotemporal reconstruction from a limited number of non-time-resolved two-dimensional, two-component (2D-2C) velocity measurements (c.f., basic PIV). The velocity field is projected onto resolvent modes and the amplitudes and phases are optimized to satisfy statistical constraints. The velocity field can then be reconstructed in the homogeneous spatial directions as well as in time. Because the resolvent modes are derived directly from the governing Navier-Stokes equations, and statistical constraints are enforced, the reconstructed flow field is expected to be physically and statistically consistent.

For proof-of-concept tests of this method, we use DNS data for turbulent channel flow at $Re_\tau = u_\tau h/\nu = 1000$ available from the JHTDB (Graham *et al.*, 2016) as the input or the surrogate for experimental PIV measurements. Here, u_τ is the friction velocity, h is the channel half-height, and ν is kinematic viscosity. For consistency with typical PIV systems, we use only 2D-2C velocity data that is sampled uniformly in time and space. We consider reconstruction from measurements made in a single streamwise-wall normal $(x-y)$ plane as well as measurements made simultaneously in the $x-y$ and $y-z$ planes, where z is the spanwise direction. We evaluate how increasing the number of snapshots affects reconstruction performance. In addition, we compare reconstructions for two different resolvent models: one which makes use of the molecular viscosity (ν) and another that includes the eddy viscosity (ν_T) in the input-output transfer function Morra *et al.* (2019).

This work complements prior literature on resolvent-based reconstruction. Prior studies have successfully reconstructed the velocity field from time-resolved point measurements in band-limited flows such as inclined square cylinder wakes (Gómez *et al.*, 2016) and jets (Beneddine *et al.*, 2017) by projecting the velocity field on to resolvent modes. Recent studies reconstruct the full 3D velocity field for turbulent channel flow from spatiotemporally-resolved velocity field snapshots at a single wall-normal location (Illingworth *et al.*, 2018) or from wall-based measurements of shear stress and pressure (Amaral *et al.*, 2021). The key distinction in the present work is the use of limited measurements that are not spatially or temporally resolved to reconstruct a broadband turbulent flow.

METHODS

Resolvent-based reconstruction

In the resolvent framework, the Navier-Stokes equations are reformulated into a linear forcing-response system that in-

terprets the nonlinear term as a forcing and the velocity and pressure fields as the response (McKeon, 2017). For turbulent channel flows that are homogeneous in the streamwise (x) and spanwise (z) directions and statistically stationary in time (t), the governing equations can be Fourier transformed and the forcing-response system can be formulated independently for each wave-number frequency triplet $\mathbf{k} = \{k_x, k_z, \omega\}$. The transfer function between the input forcing and output state variables for each $\mathbf{k}$ is the resolvent operator $\mathbf{H_k}$. A gain-based decomposition of the resolvent operator then identifies high gain forcing and response modes. The response modes are travelling wave structures, which serve as the candidate basis functions onto which we project the velocity field. An eddy viscosity model is included in resolvent operator to incorporate the effect of Reynolds stresses (Morra *et al.*, 2019). Resolvent modes are then computed for a channel geometry for the following streamwise and spanwise wavelength (λ_x, λ_z) and mode speed (c^+) ranges: $0.125 < |\lambda_x|/h < 16$, $0.125 < \lambda_z/h < 16$, and $0 < c_p^+ \leq 22.63$. A database of 53040 resolvent modes is compiled. To limit database size only rank 1 modes are used.

We assume that the total velocity field can be represented as a linear combination of the resolvent modes:

$$\hat{\mathbf{u}}(x,y,z,t) = \Re\left(\sum_{\mathbf{k}} \alpha_{\mathbf{k}} \underbrace{\tilde{\mathbf{u}}_{\mathbf{k}}(y)\exp\left(i(k_x x + k_z z - \omega t)\right)}_{\mathbf{p_k}}\right). \quad (1)$$

Here, $\tilde{\mathbf{u}}_{\mathbf{k}}(y)$ is the resolvent mode computed for wavenumber-frequency combination $\mathbf{k} = (\kappa_x, \kappa_z, \omega)$. The complex coefficients $\alpha_{\mathbf{k}}$ determine the amplitude and phase of the mode. Note that each term in the summation comprises two basis functions and two coefficients corresponding to the real and imaginary components of $\tilde{\mathbf{u}}_{\mathbf{k}}$ and $\alpha_{\mathbf{k}}$, respectively. Thus, $M/2$ resolvent modes yield M basis functions and M coefficients.

The reconstruction problem essentially amounts to tuning the coefficients $\alpha_{\mathbf{k}}$ using measurement data. For this, the 3D flow fields for each resolvent mode, $\mathbf{p_k}$, are evaluated with the same spatial and temporal dimensions at the input data to form candidate basis functions d_m in a large database $\mathbf{D}$. For instance, for reconstruction from 2D-2C data in the $x-y$ plane, the streamwise and wall normal components of velocity (u,v) are extracted with the same spatial and temporal resolution as the PIV-like input data. The PIV-like input velocity data are now projected on to these basis functions:

$$\underbrace{\begin{bmatrix}\mathbf{u}_1\\ \mathbf{u}_2\\ \vdots\\ \mathbf{u}_N\end{bmatrix}}_{input\ \ data} \approx \underbrace{\begin{bmatrix} | & | & & | \\ d_1 & d_2 & \cdots & d_M \\ | & | & & | \end{bmatrix}}_{basis\ \ functions} \underbrace{\begin{bmatrix}b_1\\ b_2\\ \vdots\\ b_M\end{bmatrix}}_{coefficients}, \quad (2)$$

or equivalently, $\mathbf{u} \approx \mathbf{Db}$. Here, $\mathbf{u}$ represents the sequence of N input velocity field snapshots reshaped into a column vector, $\mathbf{D}$ represents the database of M basis functions (or $M/2$ different resolvent modes) and $\mathbf{b}$ is a column vector of coefficients for the basis functions.

Identifying dominant resolvent modes

Standard least squares method cannot be used for the regression problem in Eq. 2 due to the limited measurement data available and the large number of candidate resolvent modes in the database, i.e., the likelihood of over-fitting. Thus, we seek a sparse solution in which only a small number of coefficients are non-zero. For this we use the FROLS algorithm (Billings, 2013), which sequentially identifies the resolvent modes that best represent the input training data and calibrates their amplitude and phase. Here, we use a slightly modified version which selects a full resolvent mode instead of the real or imaginary component of it. This allows us to reconstruct flow fields with arbitrary phase shifts between the modes. This implementation is similar to the one used in Chinta *et al.* (2022). For all the cases considered in this paper, reconstruction is carried out with the first 200 resolvent modes (or 400 basis functions) identified by the FROLS algorithm.

Enforcing statistical constraints

Although the reconstructed flow field ($\hat{\mathbf{u}} = \mathbf{Db}$) is expected to represent the input data with reasonable accuracy, there is no guarantee that the resulting flow field will be statistically sound. Thus, we solve an additional optimization problem to enforce statistical consistency. Specifically, we minimize the following composite cost function:

$$\mathscr{C} = \lambda \mathscr{C}_1 + (1-\lambda)\mathscr{C}_2 \quad (3)$$

where λ is a hyper-parameter to adjust the fit towards the velocity field or the statistics, and

$$\mathscr{C}_1 = \|\mathbf{u} - \hat{\mathbf{u}}\|_F^2 / \|\mathbf{u}\|_F^2, \quad \mathscr{C}_2 = \|\overline{\mathbf{u}^2} - \widehat{\overline{\mathbf{u}^2}}\|_2 / \|\overline{\mathbf{u}^2}\|_2, \quad (4)$$

represent cost functions for the velocity field and second-order statistics. Note that the velocity components and statistical quantities used for training can be different depending on the data available. As an example, for reconstruction from 2D-2C velocity snapshots in the $x-y$ plane, we have $\mathbf{u} = (u,v)$ and $\overline{\mathbf{u}^2} = (\overline{u^2}, \overline{v^2}, \overline{uv})$. For this case, second-order statistics for the identified and calibrated resolvent modes are given by

$$\widehat{\overline{\mathbf{u}^2}} = \begin{bmatrix}\widehat{\overline{u^2}}\\ \widehat{\overline{v^2}}\\ \widehat{\overline{uv}}\end{bmatrix} = \sum_{\mathbf{k}} \frac{|\alpha_{\mathbf{k}}|^2}{2} \Re\left(\begin{bmatrix}\tilde{u}_{\mathbf{k}}^* \tilde{u}_{\mathbf{k}}\\ \tilde{v}_{\mathbf{k}}^* \tilde{v}_{\mathbf{k}}\\ \tilde{u}_{\mathbf{k}}^* \tilde{v}_{\mathbf{k}}\end{bmatrix}\right) \quad (5)$$

where $\tilde{u}_{\mathbf{k}}$ and $\tilde{v}_{\mathbf{k}}$ respectively represent the streamwise and wall-normal components of $\tilde{\mathbf{u}}_{\mathbf{k}}$, and a superscript * denotes the complex conjugate. Note that second-order statistics for turbulent channel flow, $\overline{\mathbf{u}^2}$, can be computed directly from the measurements or obtained from other sources (including models). We use the multistart optimization routine in MATLAB to find the solution, i.e., the set of coefficients $\alpha = \{\alpha_{\mathbf{k}}\}$ that minimize the composite cost function in Eq. 3: $\alpha = \underset{\alpha'}{\arg\min}\ \mathscr{C}(\alpha')$.

Numerical Evaluation

The full DNS dataset acquired from JHTDB composes 256 snapshots obtained at intervals of $\delta t^+ = 0.0625$, for both the $x-y$ and $y-z$ planes. Following standard notation, the superscript $+$ denotes normalization with respect to u_τ and ν. Thus, the total time interval between the first and last snapshots is $T^+ = 256 \times \delta t^+ \approx 16$. For the $x-y$ plane, we use a uniformly sampled grid with $N_x \times N_y = 32 \times 64$ extending

over a region of size $2h \times h$. For the $y-z$ plane, we use a $N_y \times N_z = 64 \times 32$ grid extending over a region of size $h \times 2h$. Only the first and last DNS snapshots are used to reconstruct the flow field. The intervening snapshots are used to quantify reconstruction accuracy using separate error metrics for the observed (*trained*) variables and the unobserved (*watched*) variables. For reconstruction from 2D-2C data in the $x-y$ plane, the trained components are the velocity fields (u,v) and the statistical quantities $(\overline{u^2},\overline{v^2},\overline{uv})$. The watched variables are the spanwise velocity component and pressure (w,p), and the statistical quantities $(\overline{w^2},\overline{p^2},\overline{wp})$. Integrated error metrics for the trained and watched quantities are defined as

$$\begin{aligned}\varepsilon_{\mathbf{u}(train)} &= \frac{1}{2}\left(\frac{\|u-\hat{u}\|_F}{\|u\|_F}+\frac{\|v-\hat{v}\|_F}{\|v\|_F}\right),\\ \varepsilon_{\mathbf{u}(watch)} &= \frac{1}{2}\left(\frac{\|w-\hat{w}\|_F}{\|w\|_F}+\frac{\|p-\hat{p}\|_F}{\|p\|_F}\right),\end{aligned} \tag{6}$$

and

$$\begin{aligned}\varepsilon_{\overline{\mathbf{u}^2}(train)} &= \frac{1}{3}\left(\frac{\|\overline{u^2}-\widehat{\overline{u^2}}\|_2}{\|\overline{u^2}\|_2}+\frac{\|\overline{v^2}-\widehat{\overline{v^2}}\|_2}{\|\overline{v^2}\|_2}+\frac{\|\overline{uv}-\widehat{\overline{uv}}\|_2}{\|\overline{uv}\|_2}\right),\\ \varepsilon_{\overline{\mathbf{u}^2}(watch)} &= \frac{1}{3}\left(\frac{\|\overline{w^2}-\widehat{\overline{w^2}}\|_2}{\|\overline{w^2}\|_2}+\frac{\|\overline{p^2}-\widehat{\overline{p^2}}\|_2}{\|\overline{p^2}\|_2}+\frac{\|\overline{up}-\widehat{\overline{up}}\|_2}{\|\overline{up}\|_2}\right).\end{aligned} \tag{7}$$

Here the variables shown with a $\hat{()}$ are the reconstructed velocity or statistical components, while the unhatted variables are the DNS ground 'truth'. Similarly, for reconstructions from data in both the $x-y$ and $y-z$ planes, the trained variables are the streamwise and wall-normal velocity components (u,v) for the $x-y$ plane, and the wall-normal and spanwise velocity components (v,w) for the $y-z$ plane. Statistical constraints are imposed on the quantities ($\overline{u^2}$, $\overline{v^2}$, $\overline{w^2}$, $\overline{uv}$). The watched components are (w,p) in the $x-y$ plane and (u,p) in the $y-z$ plane. The watched statistical quantities are $(\overline{p^2},\overline{up})$. In this case, the error metrics in Eqs. 6-7 are modified to reflect the different trained and watched quantities.

Table 1. Cases discussed in this study. In the second column, ν represents resolvent analysis with the molecular viscosity while ν_T is for an eddy viscosity model. N is the number of snapshots used for training. The fourth column indicates the planes and velocity data available for training. λ is the hyper-parameter used in constrained optimization, see Eq. 3

Case	Visc. Model	N	Planes	λ
1	ν	2	x-y (u,v)	0.5
2	ν	2	x-y (u,v), y-z (v,w)	0.5
3	ν_T	2	x-y (u,v), y-z (v,w)	0.5
4	ν	2	x-y (u,v), y-z (v,w)	0.9
5	ν	8	x-y (u,v), y-z (v,w)	0.5

Cases

This paper evaluates reconstruction for the 5 different data scenarios listed in Table 1. These cases systematically evaluate reconstruction accuracy for different measurement planes, viscosity models, training snapshot numbers, as well as the hyper-parameter (λ) that sets the relative weighting for the velocity field and statistics in the cost function used for the optimization algorithm (Eq. 3).

Case 1 represents the baseline case in which reconstruction is carried out using the molecular viscosity (ν) resolvent modes from $N = 2$ snapshots obtained in the $x-y$ plane with a time interval of $T^+ \approx 16$. Case 2 builds on Case 1 to consider reconstruction from simultaneous measurements in both the $x-y$ and $y-z$ planes. Case 3 makes use of the eddy viscosity (ν_T) resolvent model for reconstruction. Case 4 considers a higher value for the hyper-parameter ($\lambda = 0.9$ vs. $\lambda = 0.5$ for the remaining cases). This emphasizes reconstruction of the velocity field. Finally, Case 5 evaluates reconstruction accuracy from $N = 8$ snapshots of the velocity field.

Reconstruction accuracy is evaluated for both the recostructions from FROLS (which does not take into account statistical constraints) and from constrained optimization separately. Since the watched variables and statistics are not used for either the FROLS or optimization, the reconstruction error for these quantities provides a sense for whether the resolvent-based reconstruction framework being developed here is able to generate volumetric reconstructions from limited planar data.

RESULTS AND DISCUSSION

Table 2. Reconstruction errors in the velocity field and statistical quantities for the trained and watched variables. For each case, the top row shows reconstruction error after the FROLS algorithm is used to identify and calibrate 200 resolvent mode amplitudes based on the training snapshots. The bottom row (in parentheses) shows reconstruction error after the optimization algorithm modifies the amplitudes to enforce statistical constraints.

Case	$\varepsilon_{\mathbf{u}(train)}$	$\varepsilon_{\mathbf{u}(watch)}$	$\varepsilon_{\overline{\mathbf{u}^2}(train)}$	$\varepsilon_{\overline{\mathbf{u}^2}(watch)}$
1	0.36	760.71	2.82×10^4	1.23×10^4
	(0.46)	(2.07)	(0.15)	(1.14)
2	0.51	1.15	12.50	224.16
	(0.60)	(1.25)	(0.30)	(1.54)
3	0.56	2.16	6.78×10^9	2.51×10^{10}
	(0.86)	(0.94)	(0.18)	(0.81)
4	0.51	1.15	12.50	224.16
	(0.54)	(1.14)	(0.49)	(1.78)
5	0.66	1.00	12.50	224.16
	(0.75)	(1.01)	(0.31)	(1.79)

Table 2 shows reconstruction errors in the trained and watched variables for the training snapshots, along with the errors for the trained and watched statistical quantities. For each case, the top row shows the error from FROLS. The second row (in parenthesis) shows the error after constrained opti-

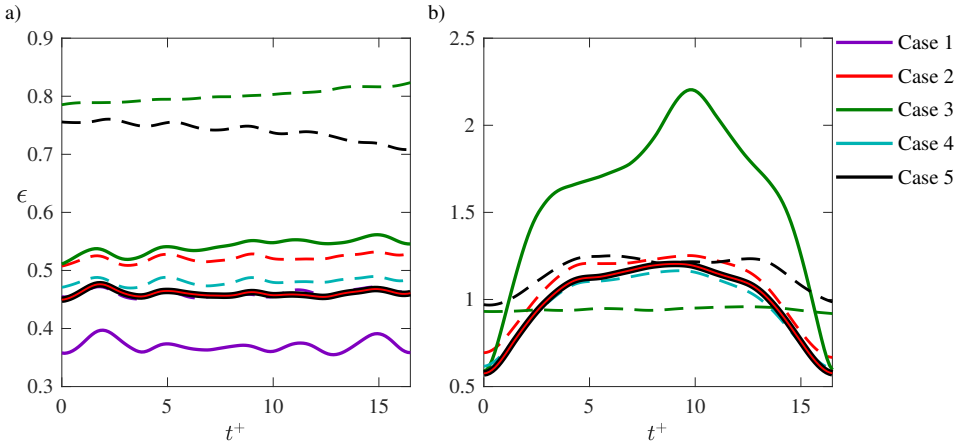

Figure 1. Error evolution for trained variables in the $x-y$ plane (a) and $y-z$ plane (b). Solid lines represent reconstructions from FROLS and dashed lines from constrained optimization.

mization. Starting with the baseline case, where a single $x-y$ plane is used, the errors for the training snapshots from FROLS are reasonably low ($\varepsilon_{\mathbf{u}(train)} < 0.4$) and the flow fields, not shown here for brevity, are qualitatively similar to the DNS truth. However, the errors for the statistical quantities are several orders of magnitude higher, $\sim O(10^4)$. After optimization the error in the statistics decreases to $O(10^{-1})$ with a slight increase from 0.36 to 0.46 in the error for the trained components of the velocity field. It is interesting to note that the error for the watched variables (w,p) decreases substantially, from 760 to 2.

Building on this case, we next use simultaneous measurements from both $x-y$ and $y-z$ planes. The error evolution for the reconstructions in the $x-y$ and $y-z$ plane are shown in Fig. 1(a) and (b), respectively. Reconstruction error for Case 2 in $x-y$ plane varies little over the time horizon, with a mean value ($\varepsilon_{\mathbf{u}(train)} \approx 0.5$) which is very close to the values reported for the training snapshots in Table 2. After optimization, the errors for both the trained and watched variables increases slightly, while the errors for the statistical quantities again decrease substantially. For instance, $\varepsilon_{\overline{\mathbf{u}^2}(train)}$ decreases from 12.5 to 0.30. It is important to note that the use of two orthogonal planes results in a significant decrease in the error for watched quantities even before optimization. The error for the watched components of velocity field changes from 760 for Case 1 to 1.15 for Case 2. Similarly, reconstruction error for the statistical quantities decreases by over two orders of magnitude for Case 2 relative to Case 1.

When the ν_T resolvent model is used (Case 3), reconstruction errors for the velocity field from FROLS are comparable to those for the ν resolvent model (Case 2). However, errors for the statistical quantities ($\sim O(10^{10})$) are several orders of magnitude larger than that for Case 2 ($\sim O(10^4)$). After optimization, the errors for the statistical quantities are reduced to $\sim O(10^{-1})$. However, the error for the velocity field rises significantly when compared to Case 2. Figure 2 compares reconstructed statistics from FROLS for Case 2 and the constrained optimization results for Cases 2 and 3 with the DNS 'truth'. As discussed before, the statistics from FROLS are several orders of magnitude higher, while the reconstructed statistics after optimization qualitatively match the DNS profiles. Note that the statistics corresponding to Case 3 are smoother and more closely approximate the DNS profiles compared to Case 2. This is consistent with the observations of Morra *et al.* (2019), who showed that the ν_T resolvent model yields better reduced representations for turbulence statistics. This is because the resolvent modes computed with an eddy viscosity model have greater support in the wall-normal direction. This results in smoother statistics. However, this also smooths out fine-scale features in the reconstructions which result in larger errors for the velocity fields.

Figure 3 compares the reconstructed flow fields after optimization for Case 2 with the corresponding snapshots from DNS. Subplots (a)-(b) show the trained velocity components in the $x-y$ plane (u,v) for one of the 2 training snapshots. Subplots (c)-(d) show the watched variables in the $x-y$ plane, i.e., spanwise velocity and pressure. Subplots (e)-(f) show the velocity fields reconstructed for a $x-y$ plane that is offset by $\Delta z/h = 0.125$ in the spanwise direction from the training snapshots. In other words, panels (c)-(f) show reconstructions for quantities that are *not* available for training the model. The reconstructions are labelled with a $\hat{(\,)}$. As expected, reconstructions for the training components (u,v) show good qualitative agreement with the DNS snapshots, though some fine-scale features are missing (see Fig. 3(a,b)). We do not see significant similarity in structure for the untrained components, i.e., (w,p) in Fig. 3(c,d). However, the magnitudes are captured. Reconstructions in the spanwise offset plane (Fig. 3(e,f)) again do not match the DNS data but the magnitudes are within range.

A comparison of Cases 1 and 2 shows that reconstruction error for the trained velocity components increases when using data from two orthogonal planes. However, errors for the watched variables and statistical quantities are reduced significantly in comparison to those obtained using data from a single plane. This suggests that using simultaneous measurements in the $x-y$ and $y-z$ planes may help in estimating unobserved (untrained) variables and potentially reconstructing volumetric flow fields from limited planar data.

Next, we consider the influence of the hyper-parameter (λ) used in Eq. 3 on errors for the velocity field and statistical quantities. Table 2 shows that, when compared to Case 2 ($\lambda = 0.5$), reconstruction errors for the velocity field for Case 4 ($\lambda = 0.9$) are slightly better after optimization. However, errors for the statistical quantities are slightly worse. A similar trend can be seen for both the trained and watched variables. This is expected from Eq. 3. A higher value for λ places greater emphasis on the loss from the flow field, which improves the velocity reconstructions but compromises the statistics.

Finally, Case 5 considers the effect of using more training snapshots. We still use 2 snapshots for training the FROLS re-

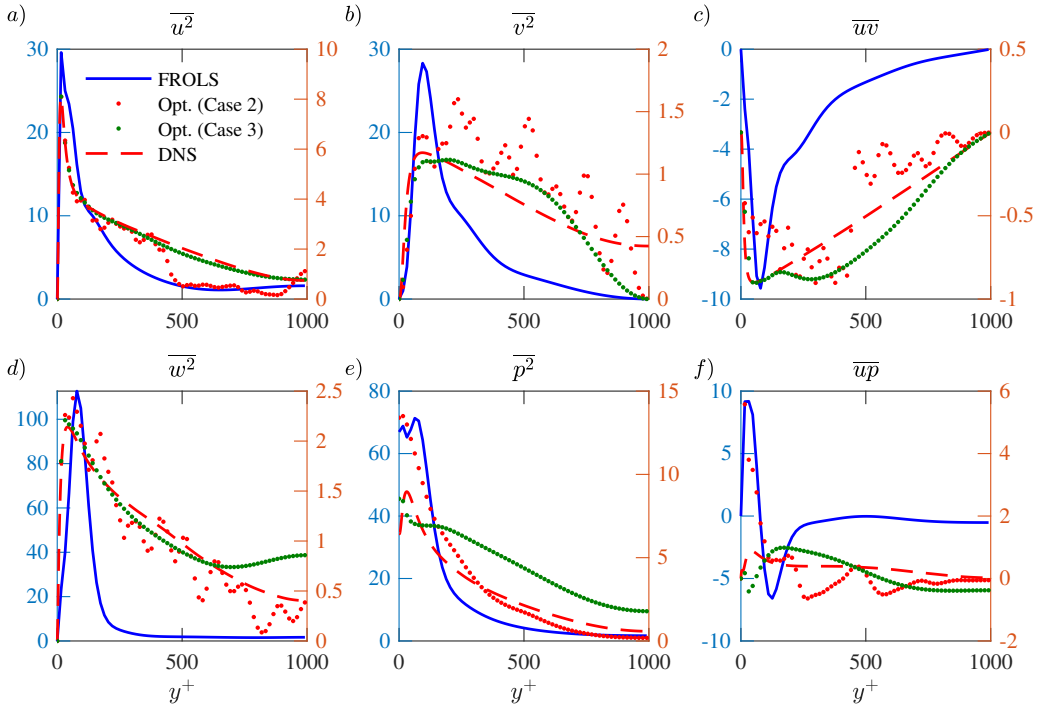

Figure 2. Reconstructed statistics from FROLS for Case 2 and constrained optimization for Cases 2 and 3. The blue scale on the left corresponds to the FROLS reconstructions with the orange scale on the right corresponds to the optimization results and DNS profiles. Note the substantial difference in magnitude from the FROLS profiles to the optimization and DNS profiles. The statistics from eddy viscosity model are smoother and more closely approximate the DNS profiles.

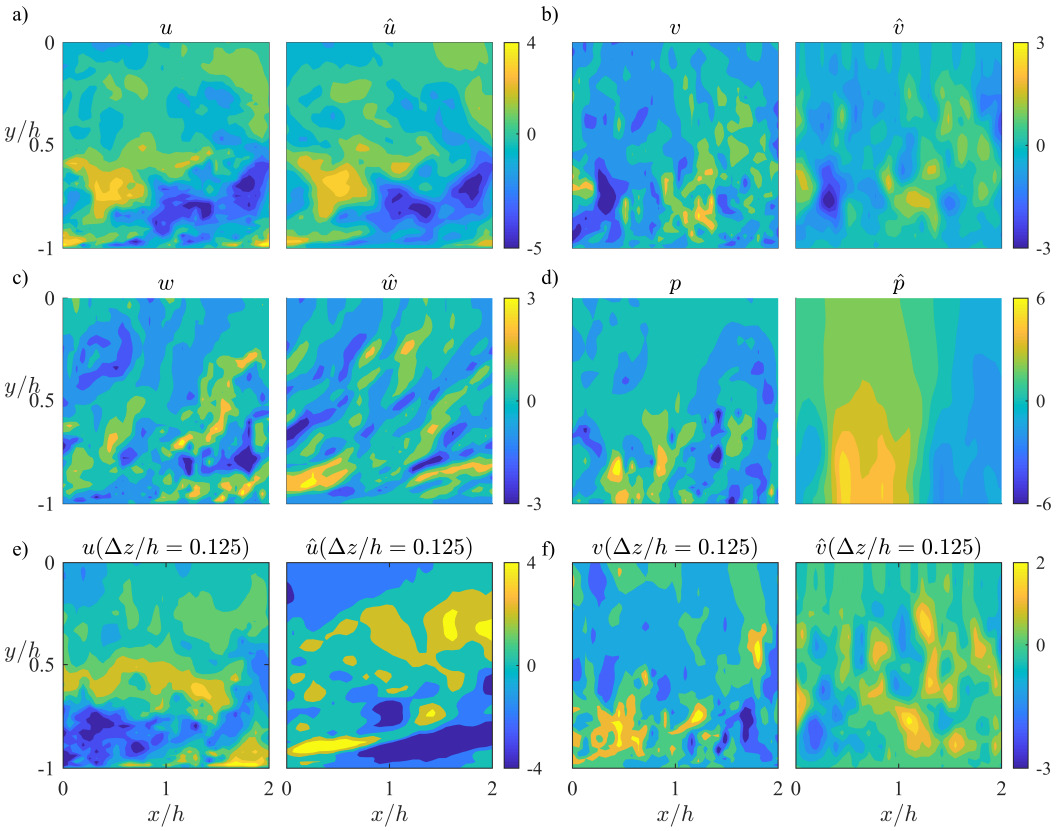

Figure 3. Reconstructed velocity and pressure fields after optimization for Case 2 are compared with DNS data. Subplots (a)-(b) show reconstructions for the observed (trained) components of velocity in the $x-y$ plane. Subplots (c)-(d) show reconstruction for the unobserved (watched) velocity and pressure fields. Subplots (e)-(f) show reconstructions at a different $x-y$ plane ($\Delta z/h = 0.125$) for the trained components (u, v)

constructions. However, after the set of 200 resolvent modes is identified, the data sequence is augmented with 6 additional snapshots obtained at the same spatio-temporal resolution. The coefficients are then optimized to minimize the loss from these 8 snapshots and the statistics. Figure 1 shows that the error after optimization is significantly increased for the $x-y$ plane when reconstruction is carried out from 8 snapshots. For the orthogonal ($y-z$) plane, reconstruction error only increases slightly (see the change in dotted vs. dashed lines). Note that the error shown in Table 2 for Case 5 considers all 8 snapshots in the data sequence. However, the time series in Fig. 1 only shows the reconstruction between the first 2 snapshots.

In general, errors for reconstructions from the $x-y$ plane are lower in comparison to errors for the $y-z$ plane. This is due to the fact that turbulent channel flow is advection-dominated. Since the flow advects in the $x-$direction, having training snapshots in the $x-y$ plane helps identify appropriate traveling wave resolvent modes. When interpolated in time using Eq. 1, these resolvent modes propagate downstream with the phase speed $c=\omega/k_x$. While the snapshots in the $y-z$ plane provide some insight into spanwise structure, they may not contain the information necessary to characterize oblique wave motion. This indicates that measurements made in the horizontal $x-z$ plane may yield improved out-of-plane reconstructions. Note that reconstruction errors generally increase with increasing input data (see Cases 1, 2, and 5). This may be attributed to the fact that all reconstructions are carried out using just 200 resolvent modes. A larger set of resolvent modes may be necessary to accurately represent the input data from multiple planes and snapshots.

CONCLUSIONS

The results presented in this paper show that projection onto resolvent modes can yield useful reconstructions for wall-bounded turbulent flows when very limited measurements are available. The FROLS algorithm efficiently identifies resolvent modes that best represent the data from a large database. However, additional constraints are needed to ensure that the reconstructions are statistically sound. Errors from FROLS reconstructions are quite high for unobserved (watched) variables and statistical quantities when 2D-2C data from a single $x-y$ plane are used as input data. After optimization to minimize a composite loss function that accounts for the input data as well as second-order statistics, these errors decrease significantly. The use of simultaneous measurements in $x-y$ and $y-z$ planes also reduces this error. The use of an eddy viscosity resolvent model leads to an increase in reconstruction error for the input velocity snapshots but greatly improves the statistics. In general, reconstruction error for unobserved quantities (e.g., out of plane velocity, pressure) reduces as statistical constraints are introduced or simultaneous measurements from multiple orthogonal planes are used. Future work will consider reconstruction from input data consistent with stereoscopic and tomographic PIV (i.e., 2D-3C and 3D-3C) as well as wall-based measurements.

ACKNOWLEDGMENTS

The authors thank Dr. Ketan Savla for fruitful discussions. VKC is grateful for financial support from the graduate school at University of Southern California through the Provost fellowship.

REFERENCES

Amaral, Filipe R, Cavalieri, André VG, Martini, Eduardo, Jordan, Peter & Towne, Aaron 2021 Resolvent-based estimation of turbulent channel flow using wall measurements. *Journal of Fluid Mechanics* **927**.

Beneddine, Samir, Yegavian, Robin, Sipp, Denis & Leclaire, Benjamin 2017 Unsteady flow dynamics reconstruction from mean flow and point sensors: an experimental study. *Journal of Fluid Mechanics* **824**, 174–201.

Billings, Stephen A 2013 *Nonlinear system identification: NARMAX methods in the time, frequency, and spatio-temporal domains*. John Wiley & Sons.

Chinta, Vamsi Krishna, Ohh, Chan-Ye, Spedding, Geoffrey & Luhar, Mitul 2022 Regime identification for stratified wakes from limited measurements: A library-based sparse regression formulation. *Physical Review Fluids* **7** (3), 033803.

Fukami, Kai, Fukagata, Koji & Taira, Kunihiko 2021 Machine-learning-based spatio-temporal super resolution reconstruction of turbulent flows. *Journal of Fluid Mechanics* **909**.

Gómez, F, Sharma, AS & Blackburn, HM 2016 Estimation of unsteady aerodynamic forces using pointwise velocity data. *Journal of Fluid Mechanics* **804**.

Graham, J, Kanov, K, Yang, XIA, Lee, M, Malaya, N, Lalescu, CC, Burns, R, Eyink, G, Szalay, A, Moser, RD *et al.* 2016 A web services accessible database of turbulent channel flow and its use for testing a new integral wall model for LES. *Journal of Turbulence* **17** (2), 181–215.

Illingworth, Simon J, Monty, Jason P & Marusic, Ivan 2018 Estimating large-scale structures in wall turbulence using linear models. *Journal of Fluid Mechanics* **842**, 146–162.

Kim, Hyojin, Kim, Junhyuk, Won, Sungjin & Lee, Changhoon 2021 Unsupervised deep learning for super-resolution reconstruction of turbulence. *Journal of Fluid Mechanics* **910**.

Krishna, C Vamsi, Wang, Mengying, Hemati, Maziar S & Luhar, Mitul 2020 Reconstructing the time evolution of wall-bounded turbulent flows from non-time-resolved PIV measurements. *Physical Review Fluids* **5** (5), 054604.

McKeon, BJ 2017 The engine behind (wall) turbulence: perspectives on scale interactions. *Journal of Fluid Mechanics* **817**.

Morra, Pierluigi, Semeraro, Onofrio, Henningson, Dan S & Cossu, Carlo 2019 On the relevance of reynolds stresses in resolvent analyses of turbulent wall-bounded flows. *Journal of Fluid Mechanics* **867**, 969–984.

Wang, Mengying, Krishna, C. Vamsi, Luhar, Mitul & Hemati, Maziar S. 2021 Model-based multi-sensor fusion for reconstructing wall-bounded turbulence. *Theoretical and Computational Fluid Dynamics* **35** (5), 683–707.